Chemical Engineering Journal 507 (2025) 160228

Contents lists available at ScienceDirect

Chemical Engineering Journal

journal homepage: www.elsevier.com/locate/cej

# Enhanced photocatalytic hydrogen evolution via ball-milled $PtO_2/TiO_2$ heterojunction photocatalyst: An alternative approach for efficient energy production☆

Ruiman Ma [a], Gareth Williams [a], Marica Muscetta [b,*], Sergio Vernuccio [c,*]

[a] School of Chemical, Materials and Biological Engineering, University of Sheffield, Sheffield, United Kingdom
[b] Dipartimento di Ingegneria Chimica, dei Materiali e della Produzione Industriale, Università di Napoli Federico II, Napoli, Italy
[c] School of Chemistry and Chemical Engineering, University of Southampton, Southampton, United Kingdom

A B S T R A C T

A novel $PtO_2/TiO_2$ heterojunction photocatalyst was synthesized via ball milling and investigated for its potential in photocatalytic hydrogen production. The effects of $PtO_2$ loading, catalyst concentration, and sacrificial agent concentration on the hydrogen evolution rate (HER) were systematically evaluated. The results indicate that increasing the $PtO_2$ concentration in the catalyst significantly enhances the hydrogen production rate, reaching a maximum value of approximately 54 $mmol \bullet h^{-1} \bullet g^{-1}$ at a $PtO_2$ concentration of 20 wt%.

The effect of the sacrificial agent concentration on the hydrogen production exhibited a Langmuir-Hinshelwood behavior with constant hydrogen production rates at sacrificial agent concentrations greater than 2.5 M. The experimental results were described by a kinetic model to shed light on the reforming mechanism. Finally, the stability of the photocatalyst was confirmed through four consecutive cycle tests.

This synergistic integration of experimental and modelling analyses provides a robust platform for uncovering mechanistic details of photocatalytic hydrogen generation using a photocatalyst synthesized through a facile preparation method.

## 1. Introduction

The extraction and consumption of fossil fuels have led to environmental challenges, including the depletion of natural resources and the increased emission of pollutants [1–3]. Hydrogen, due to its high energy density (120 $MJ \cdot kg^{-1}$) and clean combustion process, has attracted attention as a potential sustainable alternative to fossil fuels [4–6]. Among the existing hydrogen production technologies - both fossil fuel-based and renewable energy routes - solar-based approaches have garnered widespread interest. Extensive research has focused on photocatalytic water splitting [5,7] and photoreforming of organics [8–11]. The latter, which utilizes organic pollutants present in wastewater, is particularly attractive as it enables the production of hydrogen while also addressing wastewater treatment [12,13]. Methanol is the most commonly utilized sacrificial agent in photocatalytic reforming [14]. Unlike photocatalytic water splitting, which produces $H_2$ and $O_2$, photocatalytic reforming of organic compounds generates $H_2$ and $CO_2$ as its products.

Methanol adsorbed on the photocatalyst surface is oxidized by the photogenerated holes forming methoxy radical $CH_3O^{\cdot}$ and then formaldehyde $CH_2O$. Formaldehyde may either oxidize further to $CHO^{\cdot}$ and CO or hydrate to form methanediol $CH_2(OH)_2$. The latter is dehydrogenated into formic acid prior to oxidation into $CHOO^{\cdot}$ and $CO_2$. The protons generated during the oxidation steps are reduced by the photogenerated electrons to form $H_2$. As a result, methanol serves a dual role, acting both as a scavenger for photogenerated holes and as a proton donor. However, the efficiency of this process largely depends on the photocatalyst used. Generally speaking, a suitable band gap, and good chemical and physical stability are the most important characteristics to consider in the photocatalyst design [15].

To date, several semiconductors have been identified for photocatalytic hydrogen production, such as $TiO_2$ [2,16,17], ZnO [18–20], CdS [21,22], g-$C_3N_4$ [23,24]. Among these, anatase-phase titanium dioxide ($TiO_2$) is the most widely used as a photocatalyst due to its positive features (i.e., stability, abundance, environmental friendliness, and ability to absorb ultraviolet light) [25,26]. However, despite its unique physicochemical properties, limited visible light activity and high electron-hole recombination rate restrict its overall efficiency in hydrogen production, thus prohibiting the scalability of $TiO_2$-based processes for industrial applications [27,28]. To overcome these issues,

☆ This article is part of a special issue entitled: 'ISCRE 28' published in Chemical Engineering Journal.

* Corresponding authors.
*E-mail addresses:* marica.muscetta@unina.it (M. Muscetta), s.vernuccio@soton.ac.uk (S. Vernuccio).

https://doi.org/10.1016/j.cej.2025.160228

Available online 3 February 2025

significant efforts have been made to combine $TiO_2$ with other semiconductors or metallic co-catalysts to modify its light absorption capabilities and reduce the electron-hole recombination rate [29–31]. A common approach is the construction of semiconductor–semiconductor heterojunctions [32–34]. For instance, Liu et al. [35] combined CuS as a p-type semiconductor with $TiO_2$, achieving a hydrogen evolution rate (HER) approximately 17 times higher than that of pure $TiO_2$ under UV–visible light. This improvement is attributed to enhanced charge separation, leading to more efficient redox reactions. However, despite extensive research on this semiconductor, its tendency to aggregate and precipitate in aqueous media continues to limit its practical applications [36]. Similarly, the p-n heterojunction between the visible light active $Cu_2O$ ($E_g \approx 2.2$ eV) ([37]) and titania was adopted by different authors due to the possibility of facilitating the charge carrier separation as well as extending the light adsorption under the visible light range [38,39]. However, this copper-based semiconductor suffers from poor (photo)stability in aqueous solution, which restricts its practical use.

Alternatively, some noble-metal oxides such as PdO, PtO, $PtO_2$, and $IrO_2$ have recently been proposed for designing composite nanostructures in various photocatalytic applications [40–42]. Focusing on Pt-based materials, it is well-known that Pt deposited on $TiO_2$ as a co-catalyst enhances its photocatalytic efficiency [43–45]. However, the high costs of this metal and the oxidation of the produced $H_2$ by metallic Pt are typically reported as the major drawbacks [46]. Regarding the economic considerations, several techniques for recovering Pt from material waste have been developed [47,48]. Consequently, the utilization of Pt-based materials can be considered within the framework of a circular economy, utilizing materials derived from waste sources [49–51]. Furthermore, the utilization of platinum oxides (instead of metallic Pt) in photocatalytic hydrogen generation has been reported by some authors as a solution to avoid the back reactions [46]. Table 1 summarizes recent studies on photocatalytic $H_2$ generation in the presence of Pt-based photocatalysts. It is worth noting that this literature review predominantly includes works published after 2020, ensuring a focus on the latest advancements in the field. Specifically, Li and coworkers (Row 4 of Table 1) achieved a HER in the presence of PtO/$TiO_2$ photocatalyst approximately 4 times higher than the Pt/$TiO_2$ material under the same operating conditions, with negligible occurrence of the $H_2$ oxidation.

Typical methods to synthesize these photocatalysts are chemical reduction processes, in situ hydrothermal synthesis, and impregnation methods. Parayil et al. (Row 6 of Table 1) synthesized various Pt-based photocatalysts using different methods, examining how the synthesis procedure affects the distribution of Pt species on the catalyst surface. Specifically, they observed a significant amount of Pt and $PtO_2$ on the $TiO_2$ surface when the material was prepared using controlled hydrothermal synthesis. This synthesis method led to the highest HER in their study, as the close contact between the co-catalysts and $TiO_2$ enhances charge carrier propagation and reduces the electron-hole recombination rate. The coexistence of different Pt species (i.e., Pt and PtO) was also proposed by Ren and colleagues (Row 9 of Table 1). Notably, they deposited Pt/PtO phase-juncted nanodots on alkali-modified $TiO_2$ surface, producing a photocatalytic material with well-dispersed small size Pt-based cocatalyst. The photocatalyst demonstrated an exceptional photoactivity (HER = 13 mmol•$h^{-1}$•$g^{-1}$) attributed to *(i)* the presence of Pt, which facilitates efficient electron separation, and *(ii)* the presence of PtO, which improves the number of active sites of the photocatalyst and avoids $H_2$ oxidation.

Unfortunately, most of the common synthesis approaches suffer from drawbacks and limitations, such as the complexity of the methods, the high costs of the reagents and their toxicity [52]. As an alternative, ball milling is a simple, highly controllable, cost-effective, and solvent-free environmentally friendly method, which consists in the mechanical mixing of powders, either dry or in the presence of a solvent. Recently, some of the authors proposed the ball-milling approach for the preparation of $Cu_2O$-$TiO_2$ composite materials [53], as an effective, simple, and cost-efficient method for the synthesis of photocatalytic materials. Indeed, the mechanical forces involved in ball milling ensure the uniform distribution of semiconductor particles, promoting the formation of well-mixed heterojunctions. The mechanical energy generated can also introduce defects or vacancies into the crystal structure of the

**Table 1**
Recent articles on photocatalytic hydrogen production in the presence of Pt-based photocatalysts.

| | Catalyst | Preparation method | Sacrificial agent | Radiation | $H_2$ production rate ( mmol•$h^{-1}$•$g^{-1}$) | AQE or light-to-chemical energy efficiency (%) | Ref. | Year of publication |
|---|---|---|---|---|---|---|---|---|
| **1** | $PtO_x$-$TiO_2$ anatase nanotubes | Reduction process with polyvinyl alcohol and $NaBH_4$ | Methanol | 300 W Xe lamp | 0.496 | – | [59] | 2020 |
| **2** | $PtO_x/TiO_2$ | Controllable hydrolysis of the sulfuric acid solution of Pt(IV) hydroxide | Ethanol, glucose | UV LED (380 nm) | 5.3 | AQE = 1.5 % at 380 nm | [60] | 2023 |
| **3** | Pt − C/$TiO_2$ | Impregnation | 2-Propanol | 100 W Hg lamp | 2.3 | – | [61] | 2024 |
| **4** | PtO/$TiO_2$ | Chemical reduction process | Methanol | 300 W Xe lamp | 4.38 | – | [46] | 2013 |
| **5** | 0.5 wt. %Pt/$TiO_2$ | Flame spray pyrolysis | Methanol | 300 W Xe lamp | 5.52 | – | [62] | 2021 |
| **6** | Pt/$TiO_2$-$PtO_2$/$TiO_2$ | Hydrothermal synthesis, impregnation, templated phase transfer method, near monodisperse core-like method | Methanol | 300 W Xe lamp with AM 1.5 filter | 1.57 | – | [57] | 2013 |
| **7** | Pt/$TiO_2$ | In situ photodeposition | Paper (napkins) | LED (395 nm) | 0.615 | – | [44] | 2023 |
| **8** | Pt/$TiO_2$ nanorods | Hydrothermal synthesis | Methanol | UV LED (365 nm) | 12 | – | [63] | 2020 |
| **9** | Pt/PtO/$TiO_2$ | Deposition of phase-juncted Pt/PtO nanodots on hierarchically porous $TiO_2$ | Methanol | 300 W Xe lamp | 13 | AQE = 77 % at 365 nm | [64] | 2017 |
| **10** | Pt/$TiO_2$ | Wet impregnation | Methanol | 300 W Xe lamp | 3.8 | – | [65] | 2020 |
| **11** | PtOx/ $BaTiO_3$ | Impregnation | Pefloxacin | Perfectlight Labsolar-6A | 1.89 | – | [66] | 2024 |
| **12** | $PtO_x$ deposited $Fe_3O_4$-ZnO/$TiO_2$ | Green synthesis using Chamomile flowers extract | Methanol | 400 W Xe lamp with UV light filter | 0.485 | – | [67] | 2023 |
| **13** | NiS/CdS/PtOx/ $WO_3$ | Impregnation for PtOx/$WO_3$ and simple mixing with NiS/CdS | $Na_2S$/$Na_2SO_3$ | 300 W Xe lamp with AM 1.5 filter | 0.06 | – | [68] | 2023 |
| **14** | Pt doped $BaTiO_3$ | Hydrothermal synthesis | Moxifloxacin | 300 W Xe lamp with AM 1.5 filter | 1.52 | – | [69] | 2023 |
| **15** | $PtO_2/TiO_2$ | Mechanical mixing in a ball mill | Methanol | 400 W Hg lamp | 54 | AQE = 38 % $\eta$ = 15.6 % | This study | 2025 |

materials, serving as active sites for photocatalysis [53–55].

In this context, this study proposes the use of a ball milling method to combine platinum oxide ($PtO_2$), as a p-type semiconductor with a narrow band-gap (1.84 eV) [56,57], with $TiO_2$, as a n-type semiconductor [58] to form a heterojunction photocatalyst for hydrogen generation under UV–visible light irradiation. The photocatalysts were subjected to a physicochemical characterization and tested to evaluate HER by varying the catalyst load, the $PtO_2/TiO_2$ ratio, and the concentration of the sacrificial agent. Furthermore, the (photo)stability and the recyclability of the material was examined in four consecutive photocatalytic runs. Both the apparent quantum efficiency (AQE) and the light-to-chemical energy efficiency were estimated to facilitate a comparison of the obtained results with those reported in the existing literature. Finally, the mechanistic details of the process were elucidated through the development of a kinetic model.

## 2. Experimental

### 2.1. Materials

Titanium (IV) oxide (anatase nanopowder, particle size $< 25$ nm, density 3.9 g•mL$^{-1}$, specific surface area 45–55 m$^2$•g$^{-1}$, 99.7 %), platinum (IV) oxide (surface area $\geq 75$ m$^2$·g$^{-1}$) and methanol (99 %) were purchased from Sigma Aldrich. All reagents were used as received. Doubly glass–distilled water was used throughout this study.

### 2.2. Preparation and characterization of the photocatalyst

The heterojunction photocatalyst samples were prepared using a ball milling method. Specific quantities of $PtO_2$ and $TiO_2$ were mixed in various ratios (0–30 %) and ball-milled at 200 rpm for 1 min in a planetary mill (PM100, RETSCH) equipped with an agate mortar (50 mL) and 10 agate balls (10 mm) [53].

The synthesized catalyst morphology was characterized using a scanning electron microscope (SEM, FEI Inspect F-50) under 20 kV of electron beam with 3.5 spot size. An energy-dispersive X-ray (EDS) spectrometer integrated with the SEM instrument was utilized to analyze the distribution of $PtO_2$ on $TiO_2$ in the photocatalyst. The BET surface areas were analyzed according to the $N_2$ adsorption–desorption isotherms (Micromeritics 3Flex). Each sample was analyzed using X-ray diffraction (XRD) with a PANalytical Aeris diffractometer. The measurements were conducted using Cu-Kα radiation ($\lambda = 0.154$ nm) at an accelerating voltage of 40 kV and a current of 35 mA. The data were collected over a 2θ range from 10° to 100°, with a scan step size of 0.02°. The data were collected and referenced to the instrument database for phase analysis.

The diffuse reflectance spectra (DRS) of the powder samples were obtained using a UV–vis spectrometer (Agilent Cary 5000), equipped with a diffuse reflectance accessory (Harrick Scientific Praying Mantis™ ) in the range 230–850 nm.

Photoluminescence (PL) spectra were recorded at room temperature using a fluorometer performance benchtop model (Horiba FluoroMax® -4 Spectrofluorometer). The measurements were conducted with an excitation wavelength of 300 nm, and emission spectra were recorded from 350 to 580 nm. The slit widths were 12 nm, with an integration time of 0.5 s.

### 2.3. Photoactivity test

Photocatalytic experiments were carried out at ambient temperature in an annular glass batch reactor with a capacity of 300 mL and a height of 40 cm, as previously described [70]. The reactor was equipped with a magnetic stirrer (1200 rpm) and a lamp housed in a quartz jacket. The stirring rate was chosen to ensure uniform mixing of the reaction solution and verify the absence of external mass transfer resistances (Fig. S1).

A 400 W medium-pressure Hg lamp (Photochemical Reactors Ltd) was utilized as the radiation source. A schematic illustration and a photograph of the photocatalytic reactor are included in Fig. S2. The lamp emits primarily at wavelengths of 302, 313, 334, and 366 nm in the UV spectrum, and at 406 and 436 nm in the visible spectrum (manufacturer's data). The effective irradiances ($I_{\lambda_i}$) emitted by the lamp were measured using a photo-radiometer (Delta OHM, HD2102.1) equipped with two probes to detect light in the wavelength ranges of 0–400 nm and 400–1000 nm, as described in the Supporting Information (Fig. S3). Specifically, $I_{\lambda_i}$ at wavelength of 302, 313, 334, 366, 406, and 436 nm are $1.17 \times 10^{-6}$, $3.19 \times 10^{-6}$, $3.41 \times 10^{-7}$, $6.97 \times 10^{-6}$, $3.04 \times 10^{-5}$ and $6.62 \times 10^{-5}$ Ein•s$^{-1}$, respectively. A cut-off filter was employed to shield the radiation with a wavelength below 300 nm.

To prevent any undesired temperature increases in the reactor, cooling water at a fixed temperature (25 °C) was continuously circulated through the lamp jacket during the whole reaction process. In a typical experiment, a specific quantity of catalyst (0–1500 ppm) was suspended in unbuffered doubly distilled aqueous solution (0.3 L) containing methanol (0–2.5 M) as a sacrificial agent. To ensure an oxygen-free environment within the reactor, nitrogen gas was bubbled through the solution for 40 min, prior to commencing the photocatalytic experiment, effectively preventing any interaction between dissolved oxygen and photogenerated electrons. Nitrogen was continuously supplied at a rate of 1 L•min$^{-1}$ throughout the entire duration of the photocatalytic experiment. To assess the reusability of the material, the photocatalyst was separated from the reaction mixture by centrifugation after some photocatalytic experiments, dried for 24 h under air atmosphere, and utilized in the subsequent cycle. Gas samples were taken at different time intervals using 1 L Tedlar gas sampling bags and analyzed with a gas chromatograph (Thermo Scientific Trace 1310). The chromatograph was equipped with a HS-Q column (2 m, 60/80 mesh) and a thermal conductivity detector (TCD). Argon was used as the carrier gas throughout the analysis.

## 3. Results and discussion

After the preparation of the composite photocatalytic materials, the solid samples were subjected to a physicochemical characterization (Section 3.1). The hydrogen generation efficiency of the synthesized $PtO_2/TiO_2$ heterojunction photocatalyst was evaluated across varying catalyst loadings and $PtO_2$-to-$TiO_2$ ratios. Additionally, the impact of the sacrificial agent concentration on the hydrogen production, along with the catalyst recyclability and stability was examined (Section 3.2). The experimental findings were validated and mechanistically interpreted through the development of a kinetic model (Section 3.3).

### 3.1. Photocatalyst characterization

The surface morphology and compositional information of the catalysts with 5 wt%, 10 wt% and 30 wt% $PtO_2$ concentration, were examined using SEM and EDS. Loading anatase nanoparticles with $PtO_2$ at low (Fig. 1 **(a)**), medium (Fig. 1 **(b)**) and high (Fig. 1 **(c)**) concentrations results in the formation of localized $PtO_2$ clusters deposited on the $TiO_2$ surface, particularly at the highest concentration of Pt-based oxide. Fig. S4 presents higher-magnification SEM and EDS images of the catalysts containing 5 wt% and 30 wt% $PtO_2$, alongside images of bare $TiO_2$. Bare anatase nanoparticles are mostly irregularly shaped and tightly packed together, with relatively smooth surfaces.

The XRD patterns of $PtO_2/TiO_2$ composites with different $PtO_2$ concentrations, as well as bare anatase $TiO_2$ and bare $PtO_2$ are shown in Fig. 2 **(a)**. The primary characteristic diffraction peaks of bare anatase appear at $2\theta = 25.3°$, 37.9°, and 48.0°, corresponding to the (101), (004), and (200) crystal planes, respectively, according to JCPDS card number 84–1285. The characteristic diffraction peaks of bare hexagonal phase of α-$PtO_2$ are observed at $2\theta = 21.6°$, 33.5°, and 59.7°, corresponding to the (001), (100), and (110) crystal planes, respectively,

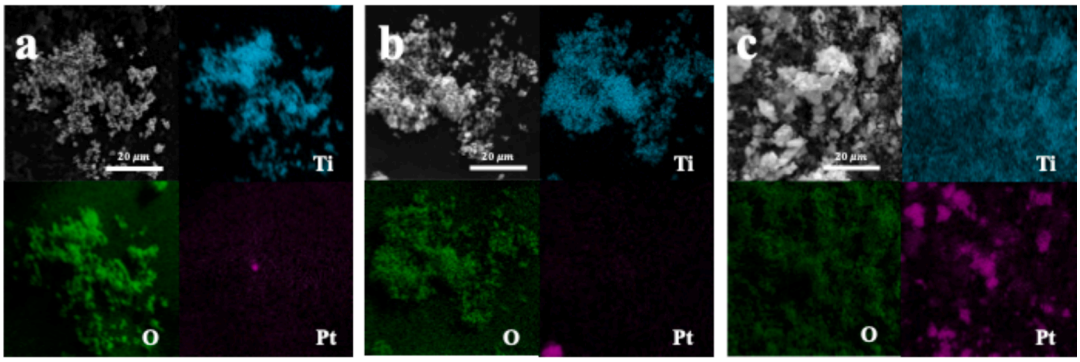


**Fig. 1.** (a) 5 wt% $PtO_2/TiO_2$ SEM images and Ti/O/Pt EDS elemental mapping images. (b) 10 wt% $PtO_2/TiO_2$ SEM images and Ti/O/Pt EDS elemental mapping images. (c) 30 wt% $PtO_2/TiO_2$ SEM images and Ti/O/Pt EDS elemental mapping images.

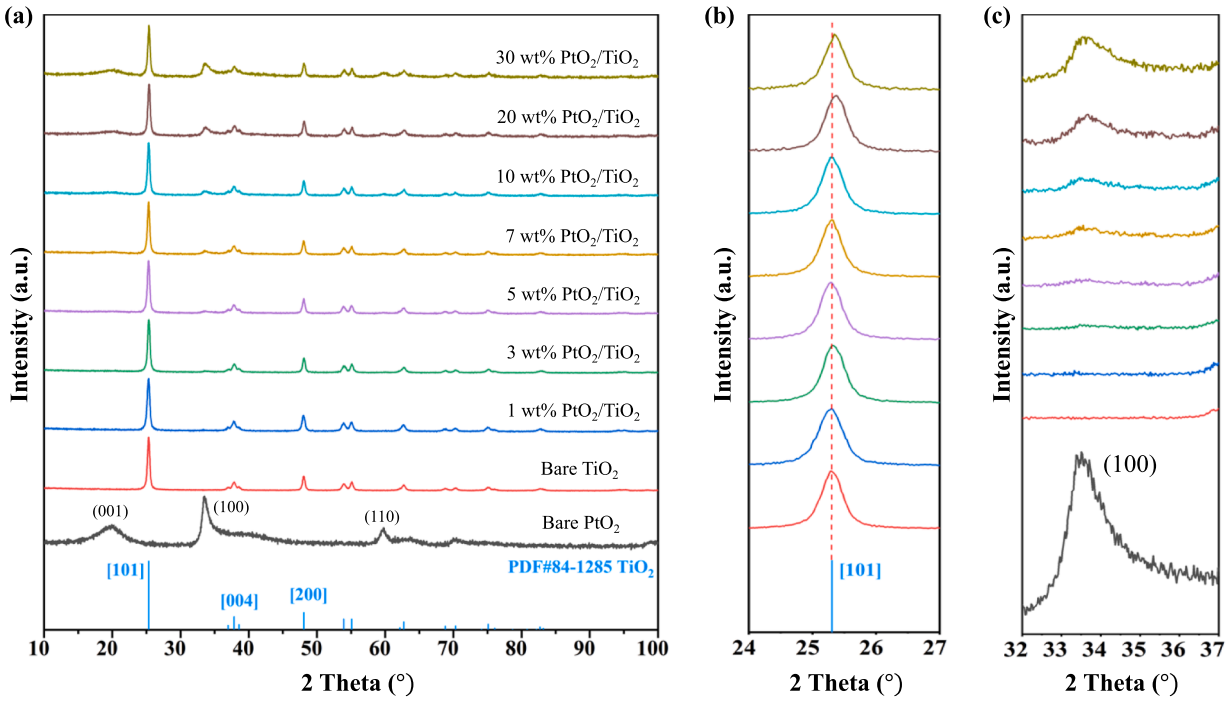


**Fig. 2.** XRD patterns of (a) bare $PtO_2$, bare $TiO_2$, and $PtO_2/TiO_2$ composite materials (1, 3, 5, 7, 10, 20, 30 wt%), (b) changes of 101 crystal plane with increasing $PtO_2$ content and (c) changes of 100 crystal plane with increasing $PtO_2$ content.

based on JCPDS card number 04–002-4419. With an increase in $PtO_2$ content from 1 to 30 wt%, a gradual increase in the intensity of the characteristic $PtO_2$ peak is observed (Fig. 2 **(c)**). No additional peaks ascribable to metallic Pt (JCPDS card number 04–0802) was detected in any instance.

Additionally, as illustrated in Fig. 2 **(b)**, increasing $PtO_2$ concentration induces a slight shift of the $TiO_2$ diffraction peaks towards higher angles, possibly due to a reduction in the overall interplanar spacing caused by $TiO_2$ lattice defects introduced through $PtO_2$ incorporation [71,72].

The PL spectra display characteristic emission bands that are commonly associated with the recombination of photogenerated charge carriers in a photocatalyst [57]. Fig. 3 shows the emission spectra of bare anatase $TiO_2$ and $PtO_2/TiO_2$ composites with different concentrations of $PtO_2$. The data reveal broad emission peaks in the wavelength range of 400–500 nm for all samples, which is typical for $TiO_2$-based materials, generally attributed to the near band edge emission or defect-related luminescence [73,74]. The intensity of the PL emission decreases compared to bare $TiO_2$ as the $PtO_2$ content increases. This quenching effect in PL intensity with increasing $PtO_2$ content suggests that the incorporation of $PtO_2$ in the photocatalyst improves the separation of photogenerated electron-hole pairs. This effect is likely due to the formation of heterojunctions at the $PtO_2/TiO_2$ interface, which facilitates charge transfer and reduces the likelihood of charge recombination [75,76].

Fig. 4 **(a)** presents the UV–vis DRS of $PtO_2/TiO_2$ composite materials with different $PtO_2$ loadings, along with bare $TiO_2$. The results reveal that $PtO_2$ loading moderately influences the optical absorption properties of the $PtO_2/TiO_2$ composite materials. All samples exhibit a pronounced absorption edge below 400 nm in the UV region, while the majority of the light in the visible spectrum is reflected. This behavior is characteristic of the intrinsic band gap absorption of $TiO_2$ [77]. Increasing the concentration of $PtO_2$ in the composite material slightly broadens the absorption edge into the visible region ($\lambda > 400$ nm), suggesting moderately improved activity of the materials under visible light irradiation [78,79].

Fig. 4 **(b)** presents the Tauc plots derived from the DRS data using the Kubelka-Munk function to estimate the optical band gap energy of the materials. The band gap for all catalysts is approximately 3.24 eV indicating that increasing $PtO_2$ concentration does not significantly alter

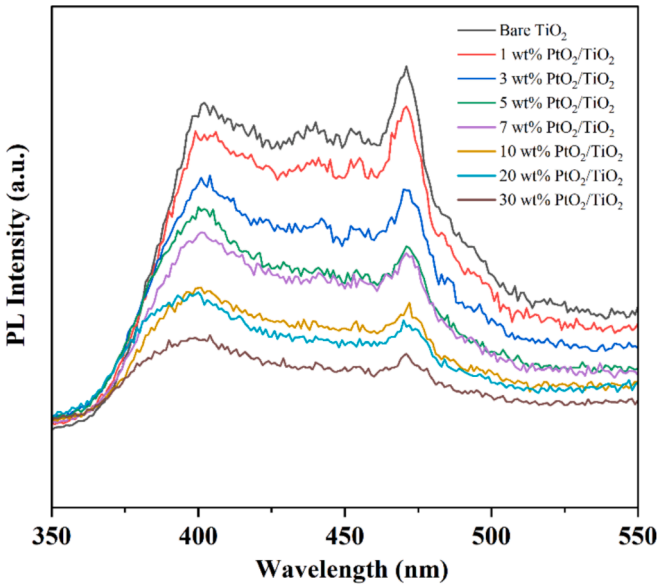


**Fig. 3.** Photoluminescence emission spectra of $PtO_2/TiO_2$ composite materials (1, 3, 5, 7, 10, 20, 30 wt%); bare $TiO_2$ is also shown for comparison.

the band gap of the material.

Table 3 compares the specific surface area ($S_{BET}$), pore volume, and average pore diameter of bare anatase and $PtO_2/TiO_2$ composite materials with different $PtO_2$ concentrations. The data show a slight increase in specific surface area with increasing $PtO_2$ loading. No significant changes were detected in the pore volume with the increase of $PtO_2$ concentration.

### 3.2. Photocatalytic experiments

The typical length of the experimental runs conducted in this work is 4 h. Each experimental run was repeated twice to ensure reproducibility of the results. A hydrogen evolution rate was calculated for each run as an average value over the time interval, after stabilization of the signal (time > 60 min). It is worth noting that the results presented below were obtained as the average of the two repeated experimental runs. An exemplary time-dependent hydrogen production rate versus time plot for a typical run has been included in Fig. S5.

Fig. 5 shows the HER obtained as a function of $PtO_2$ concentration in the composite photocatalyst, using methanol as a sacrificial agent. The hydrogen generation rate increases sharply with increasing $PtO_2$ concentration between 0 and 20 wt%, reaching a maximum value of approximately 54 mmol•$h^{-1}$•$g^{-1}$ at a $PtO_2$ concentration of 20 wt%. A further increase of $PtO_2$ concentration does not result in an enhancement of the $H_2$ production rate, likely due to the excessive coverage of $TiO_2$ and the formation of localized $PtO_2$ clusters deposited on the $TiO_2$ surface (as observed in SEM images), which is mainly responsible of the photocatalytic hydrogen production. Indeed, it is worth noting that experiments conducted using bare $PtO_2$ as a photocatalyst under the same operating conditions resulted in negligible hydrogen productions. The enhancement of the photocatalyst performance can be attributed to the effect of the formation of the heterojunction between $PtO_2$ and $TiO_2$, which reduces the recombination rate of electron-hole pairs as indicated by the PL analysis reported in the previous section.

Fig. 6 presents the hydrogen production rate recorded at varying catalyst loadings. Increasing the catalyst concentration from 0 to 700 ppm results in a rise in the HER. Beyond this concentration the hydrogen production rate stabilizes or slightly declines. This behavior may be ascribed to the partial sedimentation of the particles in the reaction mixture, as well as to the scattering effects of the incident radiations by the photocatalytic material [53].

As widely reported in literature [39,80–82] the photocatalytic

**Table 3**
BET surface area ($S_{BET}$), pore volume, and average pore diameter for bare anatase and $PtO_2/TiO_2$ composite materials.

| Photocatalyst | $S_{BET}$ ($m^2 \cdot g^{-1}$) | Pore volume ($cm^3 \cdot g^{-1}$) | Average pore diameter (nm) |
|---|---|---|---|
| Bare Anatase | 72.6 | 0.30 | 21.1 |
| 1 wt% $PtO_2/TiO_2$ | 68.7 | 0.28 | 20.6 |
| 3 wt% $PtO_2/TiO_2$ | 71.1 | 0.29 | 21.5 |
| 5 wt% $PtO_2/TiO_2$ | 73.0 | 0.29 | 18.7 |
| 7 wt% $PtO_2/TiO_2$ | 74.3 | 0.30 | 20.2 |
| 10 wt% $PtO_2/TiO_2$ | 75.6 | 0.27 | 17.7 |
| 20 wt% $PtO_2/TiO_2$ | 76.7 | 0.31 | 20.7 |
| 30 wt% $PtO_2/TiO_2$ | 78.7 | 0.32 | 19.9 |

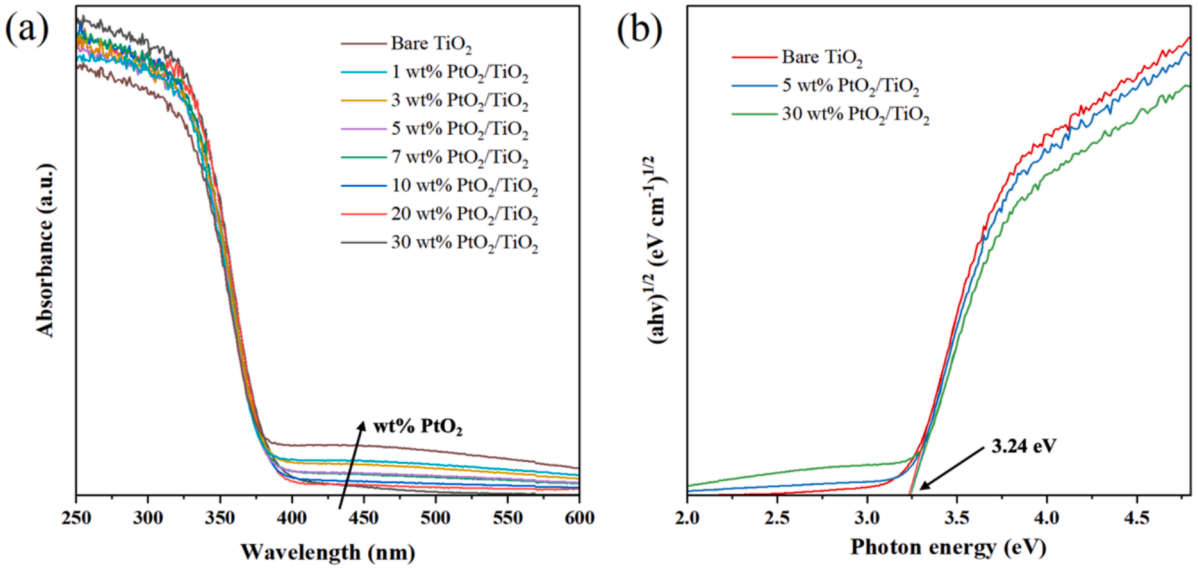


**Fig. 4.** UV–vis absorption spectra of $PtO_2/TiO_2$ composite materials (a) and corresponding Kubelka-Munk function vs. photon energy of bare $TiO_2$, 5 wt% $PtO_2/TiO_2$, and 30 wt% $PtO_2/TiO_2$ (b).

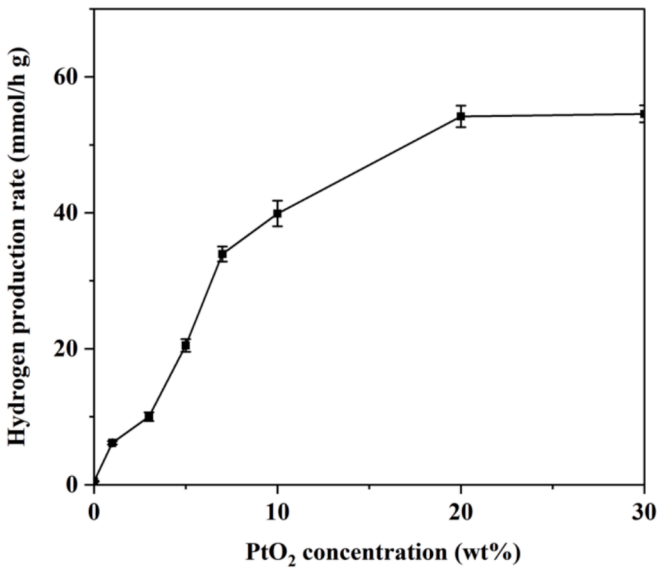


**Fig. 5.** Effect of the $PtO_2$ concentration in the $PtO_2/TiO_2$ composite materials on the hydrogen production rate after 3 h of irradiation. Experimental conditions: [Methanol] = 2.5 M; catalyst load = 500 ppm; T = 25℃; P = 1 atm; pH ≈ 4.5.

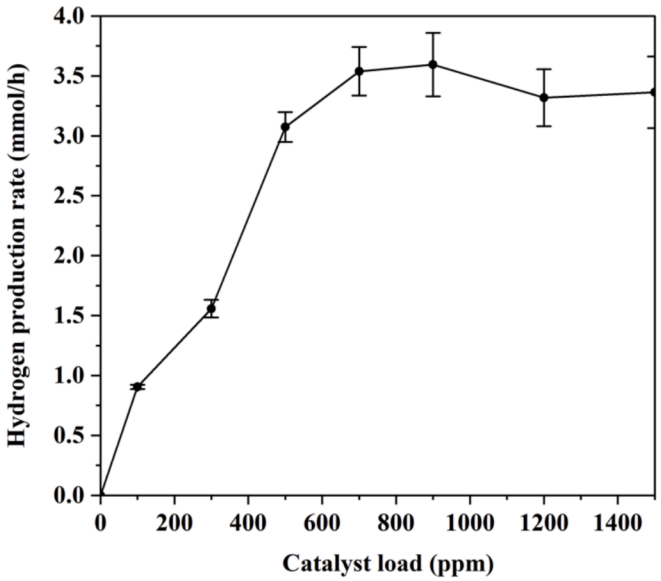


**Fig. 6.** Effect of the catalyst load on the hydrogen production rate after 3 h of irradiation. Experimental conditions: [Methanol] = 2.5 M; $[PtO_2]/[TiO_2]$ = 5 wt%; T = 25℃; P = 1 atm; pH ≈ 4.5.

hydrogen production is strongly affected by the initial concentration of the sacrificial agent in the reaction solution. Fig. 7 shows the hydrogen production rate as a function of methanol concentration, which follows a typical Langmuir-Hinshelwood behavior. At low methanol concentrations the reaction rate is limited by the availability of methanol molecules, as indicated by the sharp increase in hydrogen production rate. Once the methanol concentration reaches approximately 2.5 M, further increases in concentration do not significantly affect the reaction rate.

To assess the photostability and reusability of the $PtO_2/TiO_2$ photocatalyst, the material was tested and recovered, as described in the experimental section, over four consecutive reaction cycles, each lasting six hours. As illustrated in Fig. 8, the photocatalytic activity remains consistent after four cycles, demonstrating the excellent (photo)stability and reusability properties of the $PtO_2/TiO_2$ system.

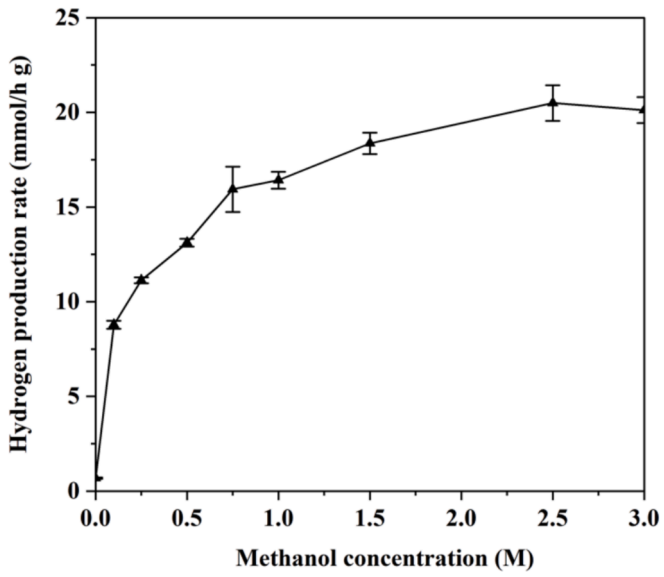


**Fig. 7.** Effect of the methanol concentration on the hydrogen production rate after 3 h of irradiation. Experimental conditions: $[PtO_2]/[TiO_2]$ = 5 wt%; Catalyst load = 500 ppm; T = 25℃; P = 1 atm; pH ≈ 4.5.

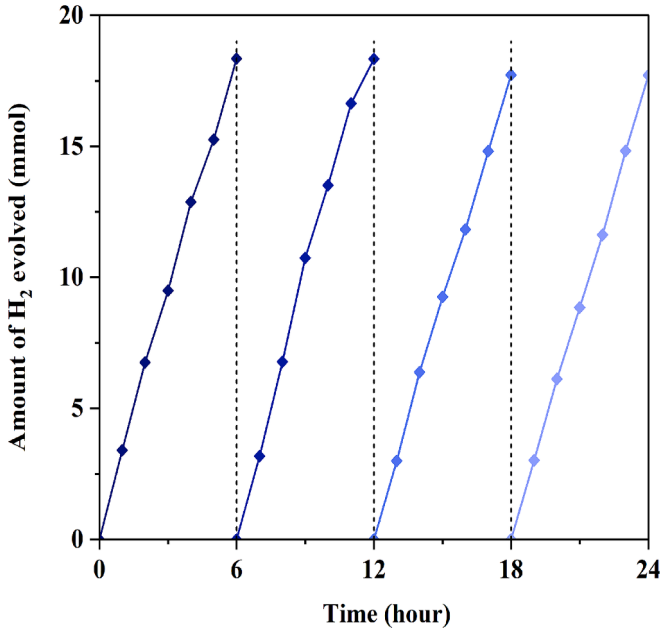


**Fig. 8.** Reusability and stability test of the $PtO_2/TiO_2$ composite materials for hydrogen production. Experimental conditions: [Methanol] = 2.5 M; $[PtO_2]/[TiO_2]$ = 5 wt%; Catalyst load = 500 ppm; T = 25℃; P = 1 atm; pH ≈ 4.5.

The analyses conducted above indicate that operating parameters such as catalyst load, methanol concentration, and $PtO_2/TiO_2$ ratio significantly influence the hydrogen productivity. Notably, the HER observed in this study surpasses most values reported in recent literature data concerning photocatalytic hydrogen generation using Pt-based photocatalysts and organic compounds at similar concentrations (see Table 1). However, a direct comparison between the different results reported in the literature is challenging, due to the differences in the employed light sources. In this regard, the calculation of the apparent quantum efficiency AQE ( eq. (1)) and the light-to-chemical energy efficiency $\eta$ ( eq. (2)), can be employed as possible indicators for an easier comparison between the results [83]:

$$AQE = \frac{2r_{H_2}}{P} \tag{1}$$

$$\eta = \frac{r_{H_2}\left(-\Delta H^0_{comb}\right)}{P} \tag{2}$$

where $r_{H_2}$ is the hydrogen generation rate expressed as mol·s$^{-1}$. $P$ is the power of the lamp obtained as the sum of the irradiances at the different emitting wavelengths (Ein·s$^{-1}$ or W), with values reported in the experimental section. Considering the band gap of the materials and the negligible activity observed under bare visible light irradiation (data not shown), only wavelengths below 400 nm were included in the calculation. $\Delta H^0_{comb} = -282$ kJ·mol$^{-1}$ represents the variation of the standard enthalpy for the combustion of hydrogen.

Considering the highest observed HER value of 54 mmol•h$^{-1}$•g$^{-1}$, the corresponding AQE was approximately 38 %, with a light-to-chemical energy efficiency of 15.6 %. The calculated AQE and $\eta$ show competitive performance relative to those reported in the literature for similar systems, despite the limited reporting on efficiency estimates [83].

### 3.3. Kinetic model

Based on previous literature findings [39,84,85], a reaction network was constructed to provide a mechanistic understanding of the photocatalytic process. To ensure the absence of external mass transfer limitations in the experimental data used for kinetic modeling, experiments were conducted at varying stirring rates (Section S1 of the Supporting Information). Furthermore, intraparticle mass transfer resistances were assessed and found to be negligible based on the Weisz-Prater criterion (Section S6 of the Supporting Information). The $PtO_2$ concentration of the catalyst was fixed at 5 wt%, treating the composite material as a single photocatalyst with a single quantum yield and electron-hole recombination rate constant. It is evident that varying the $PtO_2/TiO_2$ ratio would alter the recombination rate and affect the adsorption of UV and visible light. Upon exposure to light, the $PtO_2/TiO_2$ photocatalyst generates electron-hole pairs, following the reaction:

$$PtO_2/TiO_2 \xrightarrow{h\nu} e^- + h^+ \tag{3}$$

With the corresponding rate expression:

$$\Gamma = \frac{\psi_{UV}}{V} \bullet Q_{UV} + \frac{\psi_{vis}}{V} \bullet Q_{vis} \tag{4}$$

$$Q_{UV} = \sum\nolimits_i I^0_{\lambda_i} \bullet \left(1 - e^{(-2.3 \bullet \varepsilon_{UV} \bullet L \bullet [PtO_2/TiO_2])}\right) \tag{5}$$

$$Q_{vis} = \sum\nolimits_i I^0_{\lambda_i} \bullet \left(1 - e^{(-2.3 \bullet \varepsilon_{vis} \bullet L \bullet [PtO_2/TiO_2])}\right) \tag{6}$$

where $\Gamma$ is the total generation rate of the electron-hole pair indicating how effectively the photocatalyst generates charge carriers under the illumination of UV and visible light; $\psi_{UV}$ and $\psi_{vis}$ are the quantum yields of the photocatalyst in the UV and visible light range, while $Q_{UV}$ and $Q_{vis}$ are the photon fluxes of UV and visible light, respectively [86]; $V$ is the volume of irradiated solution. $I^0_{\lambda_i}$ is the irradiance of the lamp at the wavelength $\lambda_i$ (indicated in Section 2); $\varepsilon_{UV}$ (583.9 M$^{-1}$cm$^{-1}$) and $\varepsilon_{vis}$ (464.2 M$^{-1}$cm$^{-1}$) are the extinction coefficients of the photocatalyst at visible and UV wavelengths (experimentally measured parameters according to Lambert–Beer's-law), $L$ is the optical pathway (1 cm).

Electrons and holes can recombine either radiatively (emitting light) or non-radiatively (releasing heat):

$$e^- + h^+ \xrightarrow{k_r} heat\ and\ light \tag{7}$$

The reaction rate for the electron/hole recombination step ($r_r$) was assumed to follow a second-order law with kinetic constant $k_r$:

$$r_r = k_r[e^-][h^+] \tag{8}$$

This reaction competes with other redox reactions occurring on the catalyst surface, reducing the overall photocatalytic efficiency.

Methanol molecules adsorb onto the active sites ($\therefore^*$) of the $PtO_2/TiO_2$ catalyst surface.

$$MeOH + \therefore^* \rightleftarrows MeOH^* \tag{9}$$

The fraction of active sites covered with reaction intermediates and products was neglected, leading to the following material balance on the catalyst active sites:

$$\vartheta_{MeOH} + \vartheta_0 = 1 \tag{10}$$

where $\theta_{MeOH}$ is the catalyst surface coverage of methanol and $\vartheta_0$ denotes the fraction of vacant sites. Consequently, the concentration of adsorbed species, $MeOH^*$, can be estimated using a Langmuir-Hinshelwood expression as:

$$[MeOH^*] = \frac{C_T K_{ads}[MeOH]}{1 + K_{ads}[MeOH]} \tag{11}$$

In this model, $K_{ads}$ ( M$^{-1}$) represents the adsorption equilibrium constant of methanol, and $C_T$ ( M) is the total concentration of catalyst active sites, calculated as:

$$C_T = N \bullet C \tag{12}$$

$N$ ( mol·g$^{-1}$) is the number of active sites per unit mass of catalyst and $C$ ( g·L$^{-1}$) is the catalyst loading.

The oxidation of methanol by a photogenerated hole leads to the formation of an adsorbed radical species $R^{\bullet *}$:

$$MeOH^* + h^+ \xrightarrow{k_h} R^{\bullet *} + H^+ \tag{13}$$

with the rate expression:

$$r_1 = k_h C_T \theta_{MeOH}[h^+] \tag{14}$$

and kinetic constant $k_h$.

Further oxidation of the methanol radical results in the formation of oxidation products $P$:

$$R^{\bullet *} + h^+ \xrightarrow{k_{h2}} P + H^+ + \therefore^* \tag{15}$$

with the rate expression:

$$r_2 = k_{h2} C_T \theta_{R\bullet}[h^+] \tag{16}$$

$k_{h2}$ is the reaction rate constant and $\theta_{R\bullet}$ is the surface coverage of the radical species.

Protons are reduced by photogenerated electrons to form molecular hydrogen:

$$H^+ + e^- \xrightarrow{k_{fast}} \frac{1}{2}H_2 \tag{17}$$

with a rate expression:

$$r_3 = k_{fast}[H^+][h^+] \tag{18}$$

This reaction was assumed to be fast and irreversible ($k_{fast} = 10^{13}$ M$^{-1}$s$^{-1}$).

A mathematical model describing the change in concentration of each species in the batch reactor was formulated as represented by Equations (19)-(25).

$$\frac{d[MeOH]}{dt} = -r_1 \tag{19}$$

$$\frac{d[h^+]}{dt} = \Gamma - r_r - r_1 - r_2 \quad (20)$$

$$\frac{d[e^-]}{dt} = \Gamma - r_r - r_1 - r_2 \quad (21)$$

$$\frac{d[R^\bullet]}{dt} = r_1 - r_2 \quad (22)$$

$$\frac{d[P]}{dt} = r_2 \quad (23)$$

$$\frac{d[H^+]}{dt} = r_1 + r_2 - r_3 \quad (24)$$

$$\frac{d[H_2]}{dt} = \frac{1}{2} r_3 \quad (25)$$

The initial concentration of methanol was set as: $[MeOH]_{t=0} = MeOH_0$, while the initial concentrations of all other species, including photogenerated electrons and holes, were set to zero. Experiments conducted under visible light irradiation alone showed no activity of the photocatalyst. Therefore, $\psi_{vis} = 0$ was assumed.

The initial value of methanol adsorption constant ($K_{ads}$) was estimated by plotting the reciprocal of the experimental hydrogen production rates versus the reciprocal of the methanol concentration as illustrated in the Supporting Information (Fig. S7).

Initial values for $k_r$, $k_h$, $k_{h2}$, and $k_{fast}$ were obtained from the literature [39,84]. The initial value for $N$ ($5.55{\cdot}10^{-4}$ mol·g$^{-1}$) was determined based on the hydroxyl surface density of commercial anatase as measured by thermogravimetric analysis, according to calculations by Soares et al. [87]. Parameter estimation (Table 4) was performed using MATLAB by minimizing the square differences between experimental and calculated hydrogen production rates. Fig. 9 shows the calculated and the experimental hydrogen production rates obtained using different initial concentrations of methanol.

To validate the kinetic model, the optimal estimates of the kinetic parameters were applied with no additional adjustment to predict the experimental results across different catalyst loadings while maintaining a constant methanol concentration. Due to the model's limitations in accounting for particle sedimentation and light scattering effects at high catalyst concentrations, comparisons were restricted to loadings between 100 and 700 ppm showing a monotonic increase of the hydrogen production rate. The comparison between the experimental and model predictions demonstrates that the model can successfully predict the hydrogen production rate under various operating conditions (Fig. 10).

## 4. Conclusions

This study presents a $PtO_2/TiO_2$ heterojunction photocatalyst, synthesized using a ball milling method, for hydrogen production through photoreforming of methanol. Comprehensive characterization techniques such as SEM, XRD, UV–Vis, and PL were employed to analyze the physical and chemical properties of the synthesized catalyst. The results showed that incorporating $PtO_2$ into $TiO_2$ enhances charge carrier separation, thereby improving the photocatalytic activity.

**Table 4**
Best estimated values of the kinetic parameters with 95 % confidence intervals.

| | |
|---|---|
| $k_r$ ($M^{-1}{\cdot}s^{-1}$) | $(3.53 \pm 0.13) \times 10^6$ |
| $k_h$ ($M^{-1}{\cdot}s^{-1}$) | $(9.47 \pm 0.40) \times 10^3$ |
| $k_{h2}$ ($M^{-1}{\cdot}s^{-1}$) | $(1.42 \pm 0.03) \times 10^4$ |
| $N$ ($mol{\cdot}g^{-1}$) | $(5.57 \pm 0.01) \times 10^{-4}$ |
| $\psi_{UV}$ ($mol{\cdot}Ein^{-1}$) | $0.27 \pm 0.03$ |
| $K_{ads}$ ($M^{-1}$) | $3.10 \pm 0.30$ |

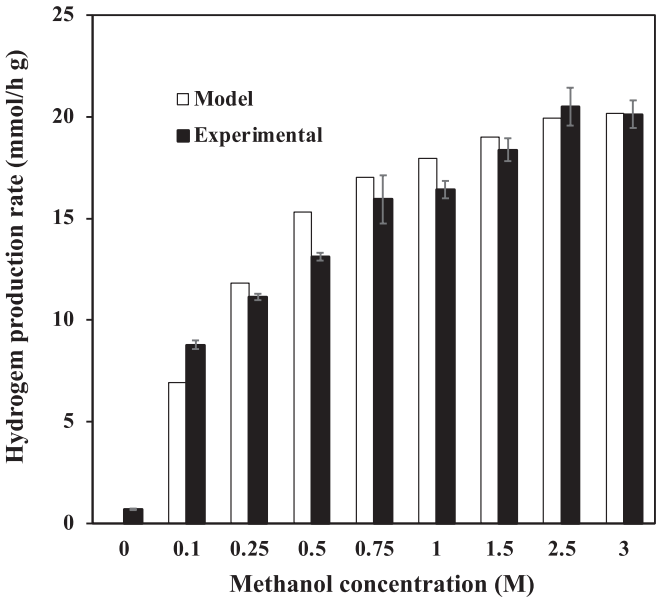


**Fig. 9.** Calculated (white) and experimental (black) hydrogen production rates at different concentrations of methanol. Experimental conditions: [$PtO_2$] = 5 wt %; Catalyst load = 500 ppm; T = 25℃; P = 1 atm; pH ≈ 4.5.

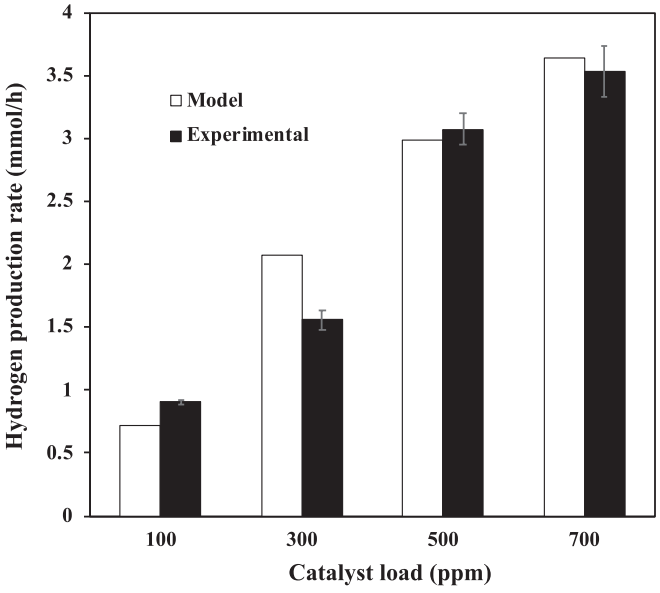


**Fig. 10.** Model prediction: Comparison of calculated (white) and experimental (black) hydrogen production rates at different catalyst loadings. Experimental conditions: [Methanol] = 2.5 M; [$PtO_2$] = 5 wt%; T = 25℃; P = 1 atm; pH ≈ 4.5.

Experimental studies revealed that the hydrogen production rate increases with the $PtO_2$ concentration in the photocatalyst, reaching a remarkable maximum value of approximately 54 mmol•h$^{-1}$•g$^{-1}$ at a $PtO_2$ concentration of 20 wt%. Beyond this point, the rate plateaued, indicating no further enhancement in the hydrogen production rate. Methanol concentration has a significant impact on hydrogen production, with the reaction rate following the Langmuir-Hinshelwood adsorption model and reaching saturation at high methanol concentrations (>2.5 M). The catalyst exhibits excellent reusability and stability, maintaining its photocatalytic efficiency over four consecutive reaction cycles without significant degradation in performance. Notably, the productivity greatly exceeds the results reported in the literature for

similar systems in the presence of Pt based materials, with an AQE of approximately 38 % in the UVA range and a light-to-chemical energy efficiency of 15.6 %.

A kinetic model was developed to describe the process at a mechanistic level and validated using the results of the experimental campaign. The model successfully predicts the relationship between hydrogen production rate, methanol concentration, and catalyst loading, providing insights into key parameters influencing the photocatalytic process.

Overall, this study highlights the potential of $PtO_2/TiO_2$ heterojunctions as efficient photocatalysts for hydrogen generation through methanol photoreforming. This system opens up new avenues for competitive production of renewable solar energy carriers in the context of a waste abatement strategy, presenting a promising strategy for sustainable energy and environmental management.

## CRediT authorship contribution statement

**Ruiman Ma:** Writing – original draft, Investigation. **Gareth Williams:** Writing – original draft, Investigation. **Marica Muscetta:** Writing – review & editing, Supervision, Data curation, Conceptualization. **Sergio Vernuccio:** Writing – review & editing, Supervision, Funding acquisition, Conceptualization.

## Declaration of competing interest

The authors declare that they have no known competing financial interests or personal relationships that could have appeared to influence the work reported in this paper.

## Acknowledgement

This paper is based upon work supported primarily by the Worldwide University Network (WUN) Research Development Fund and by the Royal Society International Exchange grant (IES\R3\203083).

## Appendix A. Supplementary data

Supplementary data to this article can be found online at https://doi.org/10.1016/j.cej.2025.160228.

## Data availability

Data will be made available on request.

## References

[1] J. Wang, W. Azam, Natural resource scarcity, fossil fuel energy consumption, and total greenhouse gas emissions in top emitting countries, Geosci. Front. 15 (2) (2024) 101757.
[2] Y. Zhang, I. Khan, M.W. Zafar, Assessing environmental quality through natural resources, energy resources, and tax revenues, Environ. Sci. Pollut. Res. 29 (59) (2022) 89029–89044.
[3] R.L. Singh, P.K. Singh, Global environmental problems, Principles and Applications of Environmental Biotechnology for a Sustainable Future (2017) 13–41.
[4] X. Xu, Q. Zhou, D. Yu, The future of hydrogen energy: Bio-hydrogen production technology, Int. J. Hydrogen Energy 47 (79) (2022) 33677–33698.
[5] D. Guilbert, G. Vitale, Hydrogen as a clean and sustainable energy vector for global transition from fossil-based to zero-carbon, Clean Technol. 3 (4) (2021) 881–909.
[6] A. Das, S.D. Peu, A comprehensive review on recent advancements in thermochemical processes for clean hydrogen production to decarbonize the energy sector, Sustainability 14 (18) (2022) 11206.
[7] S. Imran, M. Hussain, Emerging trends in water splitting innovations for solar hydrogen production: analysis, comparison, and economical insights, Int. J. Hydrogen Energy 77 (2024) 975–996.
[8] H. Nagakawa, M. Nagata, Photoreforming of organic waste into hydrogen using a thermally radiative CdO x/CdS/SiC photocatalyst, ACS Appl. Mater. Interfaces 13 (40) (2021) 47511–47519.
[9] E.I. Garcia-Lopez, A. Genco, V. Lagostina, M.C. Paganini, G. Marcì, Photocatalytic generation of H2 by photoreforming of organics in aqueous suspension of Nb2O5/C3N4 composites, Catal. Today 423 (2023) 114283.
[10] I. Rossetti, E. Bahadori, A. Villa, L. Prati, G. Ramis, Hydrogen production by photoreforming of organic compounds, Journal of Technology Innovations in Renewable, Energy 7 (2018) 55–59.
[11] D. Banerjee, N. Kushwaha, N.P. Shetti, T.M. Aminabhavi, E. Ahmad, Green hydrogen production via photo-reforming of bio-renewable resources, Renew. Sustain. Energy Rev. 167 (2022) 112827.
[12] A. Rioja-Cabanillas, D. Valdesueiro, P. Fernández-Ibáñez, J.A. Byrne, Hydrogen from wastewater by photocatalytic and photoelectrochemical treatment, Journal of Physics: Energy 3 (1) (2020) 012006.
[13] G. Iervolino, I. Zammit, V. Vaiano, L. Rizzo, Limitations and prospects for wastewater treatment by UV and visible-light-active heterogeneous photocatalysis: a critical review, Recent Advances, Heterogeneous Photocatalysis, 2020, pp. 225–264.
[14] T. Bs, R. Asapu, State of the art of methanol reforming for hydrogen generation, ChemBioEng Rev. 11 (3) (2024) 543–554.
[15] M.A. Hassaan, M.A. El-Nemr, M.R. Elkatory, S. Ragab, V.-C. Niculescu, A. El Nemr, Principles of photocatalysts and their different applications: a review, Top. Curr. Chem. 381 (6) (2023) 31.
[16] M. Murdoch, G. Waterhouse, M. Nadeem, J. Metson, M. Keane, R. Howe, J. Llorca, H. Idriss, The effect of gold loading and particle size on photocatalytic hydrogen production from ethanol over Au/TiO2 nanoparticles, Nat. Chem. 3 (6) (2011) 489–492.
[17] M. Ismael, Latest progress on the key operating parameters affecting the photocatalytic activity of TiO2-based photocatalysts for hydrogen fuel production: A comprehensive review, Fuel 303 (2021) 121207.
[18] P. Dhiman, G. Rana, A. Kumar, G. Sharma, D.-V.-N. Vo, M. Naushad, ZnO-based heterostructures as photocatalysts for hydrogen generation and depollution: a review, Environ. Chem. Lett. (2022) 1–35.
[19] G.O. Rabell, M.A. Cruz, I. Juárez-Ramírez, Hydrogen production of ZnO and ZnO/Ag films by photocatalysis and photoelectrocatalysis, Mater. Sci. Semicond. Process. 134 (2021) 105985.
[20] M.S. Hamdy, H.S. Abd-Rabboh, M. Benaissa, M.G. Al-Metwaly, A. Galal, M. Ahmed, Fabrication of novel polyaniline/ZnO heterojunction for exceptional photocatalytic hydrogen production and degradation of fluorescein dye through direct Z-scheme mechanism, Opt. Mater. 117 (2021) 111198.
[21] P. Li, X. Yan, S. Gao, R. Cao, Boosting photocatalytic hydrogen production coupled with benzyl alcohol oxidation over CdS/metal–organic framework composites, Chem. Eng. J. 421 (2021) 129870.
[22] H. Liu, J. Chen, W. Guo, Q. Xu, Y. Min, A high efficiency water hydrogen production method based on CdS/WN composite photocatalytic, J. Colloid Interface Sci. 613 (2022) 652–660.
[23] C. Prasad, H. Tang, Q. Liu, I. Bahadur, S. Karlapudi, Y. Jiang, A Latest Overview on Photocatalytic Application of g-C3N4 Based Nanostructured Materials for Hydrogen Production, International Journal of Hydrogen Energy 45 (1) (2020) 337–379.
[24] O. Polat, N. Sahiner, Recent development in solar-driven photocatalytic hydrogen production utilizing g-C3N4, Int. J. Energy Res. 46 (11) (2022) 14587–14608.
[25] D.R. Eddy, M.D. Permana, L.K. Sakti, G.A.N. Sheha, S. Solihudin, T. Hidayat, N. Takei, I.R. Kumada, Heterophase polymorph of TiO2 (Anatase, Rutile, Brookite, TiO2 (B)) for efficient photocatalyst: fabrication and activity, Nanomaterials 13 (4) (2023) 704.
[26] O.U. Akakuru, Z.M. Iqbal, A. Wu, TiO2 nanoparticles: properties and applications, TiO2 Nanoparticles: Applications in Nanobiotechnology and Nanomedicine (2020) 1-66.
[27] Y. AlSalka, O. Al-Madanat, A. Hakki, TiO2-based photocatalytic hydrogen production: How to transfer it to an applicable approach? Appl. Catal. A 662 (2023) 119287.
[28] S.R. Damkale, S.S. Arbuj, G.G. Umarji, S.B. Rane, B.B. Kale, Highly crystalline anatase TiO 2 nanocuboids as an efficient photocatalyst for hydrogen generation, RSC Adv. 11 (13) (2021) 7587–7599.
[29] J.P. Jeon, D.H. Kweon, B.J. Jang, M.J. Ju, J.B. Baek, Enhancing the photocatalytic activity of TiO2 catalysts, Adv. Sustainable Syst. 4 (12) (2020) 2000197.
[30] I. Ahmad, S. Shukrullah, M.Y. Naz, E. Ahmed, M. Ahmad, A.J. Obaidullah, A. Alkhouri, A. Mahal, Y.Y. Ghadi, An aimed review of current advances, challenges, and future perspectives of TiO2-based S-scheme heterojunction photocatalysts, Mater. Sci. Semicond. Process. 172 (2024) 108088.
[31] J. Low, C. Jiang, B. Cheng, S. Wageh, A.A. Al-Ghamdi, J. Yu, A review of direct Z-scheme photocatalysts, Small Methods 1 (5) (2017) 1700080.
[32] P. Jiménez-Calvo, V. Caps, V. Keller, Plasmonic Au-based junctions onto TiO2, gC3N4, and TiO2-gC3N4 systems for photocatalytic hydrogen production: Fundamentals and challenges, Renew. Sustain. Energy Rev. 149 (2021) 111095.
[33] A. Balapure, J.R. Dutta, R. Ganesan, Recent advances in semiconductor heterojunction: a detailed review of fundamentals of the photocatalysis, charge transfer mechanism, and materials, RSC Appl. Interfaces (2023).
[34] N. Rosman, W.N.W. Salleh, N.A.M. Razali, Heterojunction-based photocatalyst, Elsevier, Photocatalytic Systems by Design, 2021, pp. 85–130.
[35] J. Liu, X. Sun, Y. Fan, Y. Yu, Q. Li, J. Zhou, H. Gu, K. Shi, B. Jiang, P-N Heterojunction Embedded CuS/TiO2 Bifunctional Photocatalyst for Synchronous Hydrogen Production and Benzylamine Conversion, Small 20 (10) (2024) 2306344.
[36] A. Sudhaik, P. Raizada, S. Rangabhashiyam, A. Singh, V.-H. Nguyen, Q. Van Le, A. A.P. Khan, C. Hu, C.-W. Huang, T. Ahamad, Copper sulfides based photocatalysts for degradation of environmental pollution hazards: A review on the recent catalyst design concepts and future perspectives, Surf. Interfaces 33 (2022) 102182.

[37] L. Qi, M. Wang, J. Xue, Q. Zhang, F. Chen, Q. Liu, W. Li, X. Li, Simultaneous Tuning Band Gaps of Cu2O and TiO2 to Form S-Scheme Hetero-Photocatalyst, Chemistry–A, European Journal 27 (59) (2021) 14638–14644.
[38] C. Wang, J. Xiong, Z. Wen, G. Cheng, Integrated Ni (OH) 2-TiO2-Cu2O hybrids with a synergic impact of the p–n heterojunction/cocatalyst for enhanced photocatalytic hydrogen production, Ind. Eng. Chem. Res. 62 (29) (2023) 11402–11413.
[39] M. Muscetta, L. Clarizia, C. Garlisi, G. Palmisano, R. Marotta, R. Andreozzi, I. Di Somma, Hydrogen production upon UV-light irradiation of Cu/TiO2 photocatalyst in the presence of alkanol-amines, Int. J. Hydrogen Energy 45 (51) (2020) 26701–26715, https://doi.org/10.1016/j.ijhydene.2020.07.002.
[40] X. Liu, Y. Zhang, W. Zhang, G. Cheng, F. Tian, W. Li, J. Xiong, Oxidation cocatalyst/S-scheme junction cooperatively assists photocatalytic H2 production in ternary hybrid: The case of PdO@ TiO2-Cu2O, Sep. Purif. Technol. 354 (2025) 129396.
[41] M. Mokhtar, A. Shawky, Enhanced visible-light-driven H2 evolution over sol-gel prepared Nd2O3 supported with PtO nanoparticles, Ceram. Int. 48 (24) (2022) 36670–36677.
[42] D. Liu, J. Shen, Y. Xie, C. Qiu, Z. Zhang, J. Long, H. Lin, X. Wang, Metallic Pt and PtO2 Dual-Cocatalyst-Loaded Binary Composite RGO-CN x for the Photocatalytic Production of Hydrogen and Hydrogen Peroxide, ACS Sustain. Chem. Eng. 9 (18) (2021) 6380–6389.
[43] L. Li, W. Ouyang, Z. Zheng, K. Ye, Y. Guo, Y. Qin, Z. Wu, Z. Lin, T. Wang, S. Zhang, Synergetic photocatalytic and thermocatalytic reforming of methanol for hydrogen production based on Pt@ TiO2 catalyst, Chin. J. Catal. 43 (5) (2022) 1258–1266.
[44] C. Wu, L. Fang, F. Ding, G. Mao, X. Huang, S. Lu, Photocatalytic hydrogen production from water and wastepaper on Pt/TiO2 composites, Chem. Phys. Lett. 826 (2023) 140650.
[45] N.S. Ibrahim, W.L. Leaw, D. Mohamad, S.H. Alias, H. Nur, A critical review of metal-doped TiO2 and its structure–physical properties–photocatalytic activity relationship in hydrogen production, Int. J. Hydrogen Energy 45 (53) (2020) 28553–28565.
[46] Y. Hang Li, J. Xing, Z. Jia Chen, Z. Li, F. Tian, L. Rong Zheng, H. Feng Wang, P. Hu, H. Jun Zhao, H. Gui Yang, Unidirectional suppression of hydrogen oxidation on oxidized platinum clusters, Nat. Commun. 4 (1) (2013) 2500.
[47] R. Panda, M.K. Jha, J.-C. Lee, D.D. Pathak, Developed Commercial Processes to Recover Au, Ag, Pt, and Pd from E-waste, Rare Metal Technology, Springer 2021 (2021) 115–126.
[48] S. Kinas, D. Jermakowicz-Bartkowiak, P. Pohl, A. Dzimitrowicz, P. Cyganowski, On the path of recovering platinum-group metals and rhenium: A review on the recent advances in secondary-source and waste materials processing, Hydrometall. 106222 (2023).
[49] M.A. Montiel, R. Granados-Fernández, S. Díaz-Abad, C. Sáez, C.M. Fernández-Marchante, M.A. Rodrigo, J. Lobato, Towards a circular economy for Pt catalysts, Case Study: Pt Recovery from Electrodes for Hydrogen Production, Applied Catalysis b: Environmental 327 (2023) 122414.
[50] P. Trucillo, A. Lancia, F. Di Natale, Recovery of platinum from diesel catalysts by combined use of H2O2/HCl leaching and adsorption, J. Environ. Chem. Eng. 10 (3) (2022) 107730.
[51] S. Kolbadinejad, A. Ghaemi, Recovery and extraction of platinum from spent catalysts: A review, Case Stud. Chem. Environ. Eng. 7 (2023) 100327.
[52] H.S. Abd-Rabboh, M. Benaissa, M.S. Hamdy, M. Ahmed, M. Glal, Synthesis of an efficient, and recyclable mesoporous BiVO4/TiO2 direct Z-scheme heterojunction by sonochemical route for photocatalytic hydrogen production and photodegradation of rhodamine B dye in the visible region, Opt. Mater. 114 (2021) 110761.
[53] M. Muscetta, S. Al Jitan, G. Palmisano, R. Andreozzi, R. Marotta, S. Cimino, I. Di Somma, Visible light–driven photocatalytic hydrogen production using Cu2O/TiO2 composites prepared by facile mechanochemical synthesis, J. Environ. Chem. Eng. 10 (3) (2022) 107735.
[54] E. do Couto-Pessanha, V.M. Paiva, T.J. Mori, L. Soler, B. Canabarro, P. Jardim, E. D'Elia, J. Llorca, B.A. Marinkovic, Mechanochemical approach towards optimized Ni2+ spin configuration in NiO/TiO2 heterojunction with enhanced solar-driven H2 photoproduction, Int. J. Hydrogen Energy 80 (2024) 528–541.
[55] L. Yang, T. Zhang, X. Han, C. Liu, X. Zhou, Fabrication of Step-Scheme Heterojunction between Layered MoO3/TiO2 for Photocatalytic H2 Evolution and Study on the Mechanism, Adv. Sustainable Syst. 7 (1) (2023) 2200402.
[56] J. Zhensheng, X. Chanjuan, Z. Qingmei, Y. Feng, Z. Jiazheng, X. Jinzhen, Catalytic behavior of nanoparticle α-PtO2 for ethanol oxidation, J. Mol. Catal. A Chem. 191 (1) (2003) 61–66.
[57] S.K. Parayil, H.S. Kibombo, C.-M. Wu, R. Peng, T. Kindle, S. Mishra, S.P. Ahrenkiel, J. Baltrusaitis, N.M. Dimitrijevic, T. Rajh, Synthesis-dependent oxidation state of platinum on TiO2 and their influences on the solar simulated photocatalytic hydrogen production from water, J. Phys. Chem. C 117 (33) (2013) 16850–16862.
[58] H. Wang, H. Jiang, P. Huo, M.F. Edelmannova, L. Čapek, K. Kočí, Hydrogen production from methanol-water mixture over NiO/TiO2 nanorods structure photocatalysts, J. Environ. Chem. Eng. 10 (1) (2022) 106908.
[59] A. Alshehri, K. Narasimharao, PtOx-TiO2 anatase nanomaterials for photocatalytic reformation of methanol to hydrogen: effect of TiO2 morphology, J. Mater. Res. Technol. 9 (6) (2020) 14907–14921.
[60] P. Tkachenko, V. Volchek, A. Kurenkova, E. Gerasimov, P. Popovetskiy, I. Asanov, I. Yushina, E. Kozlova, D. Vasilchenko, Photocatalytic H2 generation from ethanol and glucose aqueous solutions by PtOx/TiO2 composites, Int. J. Hydrogen Energy 48 (59) (2023) 22366–22378.
[61] H. Šalipur, D. Manojlović, K. Milošević, M. Fronczak, A.G. Silva, D. Lončarević, J. Dostanić, Unraveling the solar and visible light-induced deactivation mechanism of Pt-decorated carbon/TiO2 nanocomposite in photocatalytic hydrogen production, J. Environ. Chem. Eng. 12 (3) (2024) 112862.
[62] F. Gao, Z. Xu, H. Zhao, Flame spray pyrolysis made Pt/TiO2 photocatalysts with ultralow platinum loading and high hydrogen production activity, Proc. Combust. Inst. 38 (4) (2021) 6503–6511.
[63] Y.-H. Chung, K. Han, C.-Y. Lin, D. O'Neill, G. Mul, B. Mei, C.-M. Yang, Photocatalytic hydrogen production by photo-reforming of methanol with one-pot synthesized Pt-containing TiO2 photocatalysts, Catal. Today 356 (2020) 95–100.
[64] X.-N. Ren, Z.-Y. Hu, J. Jin, L. Wu, C. Wang, J. Liu, F. Liu, M. Wu, Y. Li, G. V. Tendeloo, Cocatalyzing Pt/PtO phase-junction nanodots on hierarchically porous TiO2 for highly enhanced photocatalytic hydrogen production, ACS Appl. Mater. Interfaces 9 (35) (2017) 29687–29698.
[65] Z. Jiang, R. Qi, Z. Huang, W. Shangguan, R.J. Wong, A. Lee, Impact of methanol photomediated surface defects on photocatalytic H2 production over Pt/TiO2, Energy Environ. Mater. 3 (2) (2020) 202–208.
[66] G. Chen, Y. Ji, X. Shi, P. An, J. Zhang, Y. Li, S.F. Liu, J. Yan, Oxygen deficient BaTiO3 loading sub-nm PtOx for photocatalytic biological wastewater splitting to green hydrogen production, Chem. Eng. J. 496 (2024) 154261.
[67] S.A. Althabaiti, Z. Khan, S.M. Bawaked, S.Z. Al-Sheheri, M. Mokhtar, M.A. Malik, K. Narasimharao, PtOx deposited Fe3O4-ZnO/TiO2 nanocomposites for photocatalytic H2 production under visible light, J. Environ. Chem. Eng. 11 (5) (2023) 110615.
[68] X. Wang, Z. Zhuo, C. Shen, M. Cai, D. Li, K. Liu, S. Cao, Y. Wei, Z. Xue, S. Sun, Visible-Light Driven Z-Scheme Water Splitting over NiS/CdS/PtOx/WO3 through Modulating Redox Mediator Environments, ChemPhotoChem 7 (4) (2023) e202200211.
[69] T. Zhang, Z. Zhao, D. Zhang, X. Liu, P. Wang, Y. Li, S. Zhan, Superexchange-induced Pt-O-Ti3+ site on single photocatalyst for efficient H2 production with organics degradation in wastewater, Proc. Natl. Acad. Sci. 120 (23) (2023) e2302873120.
[70] S. Qu, R. Ma, I. Efimov, E. Hadjittofis, S. Vernuccio, K.S. Campbell, Understanding and Tuning Fe-Doping on Zn–Fe Layered Double Hydroxide Particle and Photocatalytic Properties, Adv. Energy Sustainability Res. (2025) 2400309.
[71] B. Santara, P. Giri, K. Imakita, M. Fujii, Microscopic origin of lattice contraction and expansion in undoped rutile TiO2 nanostructures, J. Phys. D Appl. Phys. 47 (21) (2014) 215302.
[72] G. Rajender, P. Giri, Strain induced phase formation, microstructural evolution and bandgap narrowing in strained TiO2 nanocrystals grown by ball milling, J. Alloy. Compd. 676 (2016) 591–600.
[73] L. Pan, S. Wang, J. Xie, L. Wang, X. Zhang, J.-J. Zou, Constructing TiO2 pn homojunction for photoelectrochemical and photocatalytic hydrogen generation, Nano Energy 28 (2016) 296–303.
[74] K.-S. Jeon, S.-D. Oh, Y.D. Suh, H. Yoshikawa, H. Masuhara, M. Yoon, Blinking photoluminescence properties of single TiO 2 nanodiscs: interfacial electron transfer dynamics, PCCP 11 (3) (2009) 534–542.
[75] A.R.K. Farhadi, N. Rahemi, S. Allahyari, M. Tasbihi, Metal-doped perovskite BiFeO3/rGO nanocomposites towards the degradation of acetaminophen in aqueous phase using plasma-photocatalytic hybrid technology, J. Taiwan Inst. Chem. Eng. 120 (2021) 77–92.
[76] Q. Wang, L. Xiao, X. Liu, X. Sun, J. Wang, H. Du, Special Z-scheme Cu3P/TiO2 hetero-junction for efficient photocatalytic hydrogen evolution from water, J. Alloy. Compd. 894 (2022) 162331.
[77] P. Cheng, Z. Yang, H. Wang, W. Cheng, M. Chen, W. Shangguan, G. Ding, TiO2–graphene nanocomposites for photocatalytic hydrogen production from splitting water, Int. J. Hydrogen Energy 37 (3) (2012) 2224–2230.
[78] Y. Hu, X. Song, S. Jiang, C. Wei, Enhanced photocatalytic activity of Pt-doped TiO2 for NOx oxidation both under UV and visible light irradiation: A synergistic effect of lattice Pt4+ and surface PtO, Chem. Eng. J. 274 (2015) 102–112.
[79] Z. Xiong, H. Wang, N. Xu, H. Li, B. Fang, Y. Zhao, J. Zhang, C. Zheng, Photocatalytic reduction of CO2 on Pt2+–Pt0/TiO2 nanoparticles under UV/Vis light irradiation: A combination of Pt2+ doping and Pt nanoparticles deposition, Int. J. Hydrogen Energy 40 (32) (2015) 10049–10062.
[80] A. Ruiz-Aguirre, J. Villachica-Llamosas, M. Polo-López, A. Cabrera-Reina, G. Colón, J. Peral, S. Malato, Assessment of pilot-plant scale solar photocatalytic hydrogen generation with multiple approaches: Valorization, water decontamination and disinfection, Energy 260 (2022) 125199.
[81] M. Muscetta, L. Clarizia, M. Race, R. Andreozzi, R. Marotta, I. Di Somma, Visible—Light Driven Systems: Effect of the Parameters Affecting Hydrogen Production through Photoreforming of Organics in Presence of Cu2O/TiO2 Nanocomposite Photocatalyst, Appl. Sci. 13 (4) (2023) 2337.
[82] Y. Zhou, J. Liu, R. Pi, Q. Liu, R. Liu, J. Yang, Performance of photocatalytic water splitting for hydrogen production using kelp as a sacrificial agent, Int. J. Hydrogen Energy 85 (2024) 683–693.
[83] S. Nandy, T. Hisatomi, T. Takata, T. Setoyama, K. Domen, Recent advances in photocatalyst sheet development and challenges for cost-effective solar hydrogen production, J. Mater. Chem. A (2023).
[84] L. Clarizia, I. Di Somma, L. Onotri, R. Andreozzi, R. Marotta, Kinetic modeling of hydrogen generation over nano-Cu (s)/TiO2 catalyst through photoreforming of alcohols, Catal. Today 281 (2017) 117–123.
[85] L. Clarizia, G. Vitiello, R. Bericat Vadell, J. Sá, R. Marotta, I. Di Somma, R. Andreozzi, G. Luciani, Effect of Synthesis Method on Reaction Mechanism for

Hydrogen Evolution over CuxOy/TiO2 Photocatalysts: A Kinetic Analysis, Int. J. Mol. Sci. 24 (3) (2023) 2004.
[86] S.E. Braslavsky, A.M. Braun, A.E. Cassano, A.V. Emeline, M.I. Litter, L. Palmisano, V.N. Parmon, N. Serpone, Glossary of terms used in photocatalysis and radiation catalysis (IUPAC Recommendations 2011), Pure Appl. Chem. 83 (4) (2011) 931–1014, https://doi.org/10.1351/PAC-REC-09-09-36.
[87] I. Soares, E. Rodrigues, T. dos Santos, E. da Silva, M. Tavares, Surface Modification Efficiency of Titanium-based Particles with an Alkyl Phosphate, NanoWorld J 3 (1) (2017) 11–17.